







## Temperature-dependent lattice dynamics in iridium

Duncan H. Moseley <sup>1</sup>, Simon J. Thébaud <sup>1</sup>, Lucas R. Lindsay,<sup>1</sup> Yongqiang Cheng,<sup>2</sup> Douglas L. Abernathy <sup>2</sup>,  
Michael E. Manley <sup>1</sup> and Raphael P. Hermann <sup>1,\*</sup>

<sup>1</sup>*Materials Science and Technology Division, Oak Ridge National Laboratory, Oak Ridge, Tennessee 37831, USA*

<sup>2</sup>*Neutron Scattering Division, Oak Ridge National Laboratory, Oak Ridge, Tennessee 37831, USA*

 (Received 6 August 2020; revised 22 September 2020; accepted 27 October 2020; published 20 November 2020)

The characterization of simple elemental systems is key to benchmarking first-principles modeling of electronic and vibrational behaviors of materials. A large body of literature has been built for most elemental systems in the periodic table. However, surprisingly little neutron work has been performed to probe the vibrational properties of iridium, likely due to its large neutron absorption cross section. Nonetheless, iridium is of significant scientific and technological interest due to large relativistic electron effects and electron-phonon coupling, particularly in strongly correlated iridate compounds. Here, we report temperature-dependent inelastic neutron scattering measurements of the vibrational properties of iridium, from which we extract key thermodynamic properties. To overcome the challenge of the large neutron absorption of iridium, we developed a simple postprocessing correction procedure. The measured densities of phonon states compare well with quasiharmonic density functional theory calculations, although the obtained experimental phonon Grüneisen parameters are much larger than expected, reaching as high as  $\gamma = 4.5$ , indicating substantial anharmonicity.

DOI: [10.1103/PhysRevMaterials.4.113608](https://doi.org/10.1103/PhysRevMaterials.4.113608)

### I. INTRODUCTION

Iridium is a  $5d$  transition metal with a Bravais lattice face-centered-cubic (fcc) structure, i.e., a single atom per primitive cell. Despite its simple structure and interesting electronic properties with large relativistic electron effects and strong electron-phonon coupling [1–3], iridium—in particular its lattice dynamics—has received surprisingly little attention experimentally. Iridium exhibits extreme corrosion resistance and thermal stability and has found application, e.g., in spark-plug electrodes and radioisotope thermoelectric generator cladding [4]. Lattice dynamics of elemental fcc and bcc transition metals have been extensively explored by inelastic neutron and x-ray scattering, which has provided a wealth of vibrational data, including density of phonon states (DPS) and phonon dispersions, for many elements as a function of temperature [5–7]. In contrast with other transition metal elements, there is a scarcity of detailed data for iridium despite strong current interest in iridium-bearing materials, such as the iridates [8–10]. The available neutron scattering data for iridium includes partial phonon dispersion relations [2,3] and a medium-resolution DPS [1], all obtained at room temperature. On the other hand, there are numerous calculations of these properties in the literature [3,11–13]. The scarcity of measured lattice dynamics data for iridium is presumably due to its exceptionally large neutron absorption cross section (425 barns; 954 barns for Ir-191, and 111 barns for Ir-193; Ir has an absorption length of 1/3 mm for 25.4-meV thermal neutrons) which impedes inelastic scattering experiments. The characterization of simple ele-

mental systems like iridium can provide key benchmarks for first-principles-based lattice dynamical calculations in heavy element systems with strong spin-orbit interactions and thus advance predictive design capabilities [1–3,12–19]. Furthermore, temperature plays a critical role in determining lattice vibrational behaviors in solids, particularly as related to anharmonicity which determines lattice thermal expansion and thermal conductivity. Other measurements have probed structural parameters, thermal expansion [20,21], elastic constants [22,23], and specific heat at constant pressure ( $C_p$ ) of iridium [24]. However, temperature-dependent phonon data are lacking, thus there is a knowledge gap in understanding iridium's thermodynamic properties such as anharmonic contributions to the heat capacity of the material.

In this work, we present temperature-dependent inelastic neutron scattering (INS) measurements of vibrational and thermodynamic properties of iridium. A simple correction procedure is introduced that accounts for the large absorption of iridium in order to remedy an imbalance in peak intensities in the experimental DPSs as compared to calculations. Once corrected, the spectra compare well with quasiharmonic density functional theory (DFT) calculations. From the DPSs, we extract thermodynamic parameters at each temperature, including the vibrational entropy, averaged force constant, internal energy, mean atomic displacement, and phonon specific heat ( $C_{ph}$ ), as well as the phonon and macroscopic Grüneisen parameters.

### II. EXPERIMENTAL DETAILS

INS spectra were collected at the ARCS beamline [25] on a  $50 \times 50$ -mm<sup>2</sup> sheet of iridium with a 250- $\mu$ m thickness oriented at  $\sim 45^\circ$  relative to the incident neutron beam;

\*hermannrp@ornl.gov

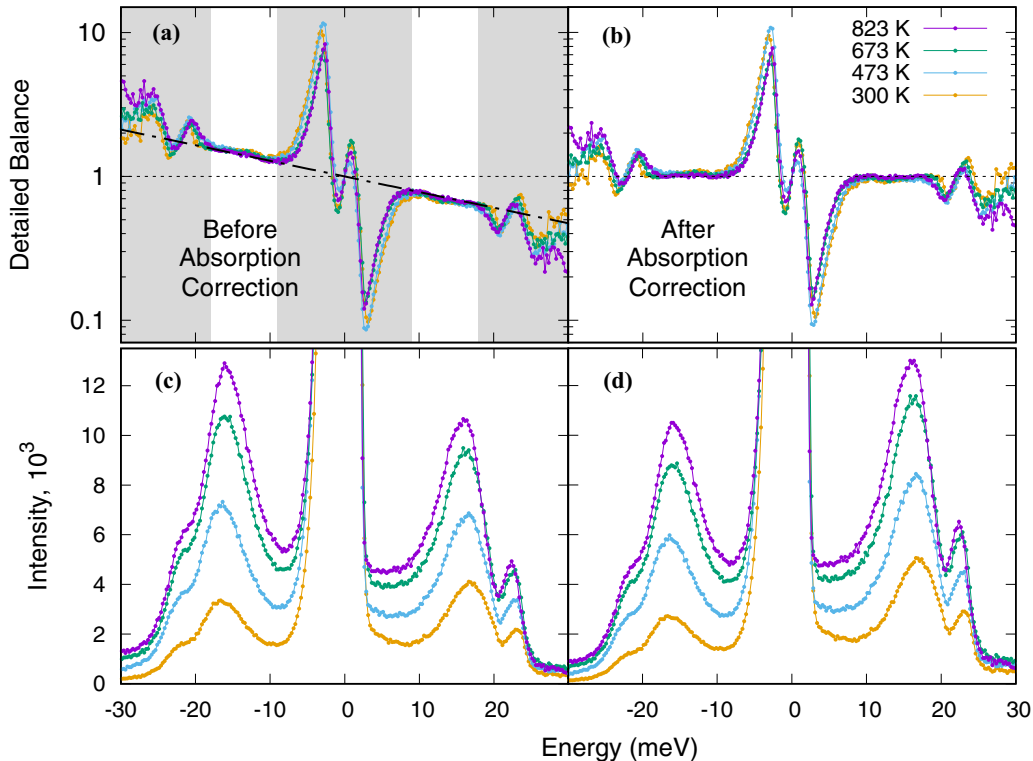


FIG. 1. Detailed balance (a),(b), in logarithmic scale, and scattering functions (c),(d) of 300–823-K INS data before (a),(c) and after (b),(d) absorption correction. The thicker slanted dashed line (a) represents the absorption correction,  $\exp(-aE)$ , which was fit to the data points in the white regions. Each scattering function (c) was then divided by the equation  $\exp(-aE/2)$  to achieve a corrected spectrum (d). Note that oscillations in the grey areas of (a) arise from the asymmetry and energy dependence in the instrumental resolution.

no sample container was needed. Data were collected using a 45-meV incident neutron energy between 10 and 250 K using a closed-cycle cryostat (CCR-16) for approximately 2 h per temperature and between 300 and 823 K using a furnace (MICAS) [26] for approximately 1 h per temperature. Background measurements were obtained using the empty CCR and furnace for the low- and high-temperature measurements, respectively. The data set was reduced to a momentum-resolved scattering function,  $S(Q, E)$  (see Fig. 5 in Appendix) by treating the data as a powder in the MSlice (DAVE) program [27] and further reduced to the scattering function  $S(E)$  by integration over the momentum transfer  $Q$  range from 1.2 to  $10 \text{ \AA}^{-1}$  [see Fig. 1(c)].

After a simple absorption correction (described below), the DPS was determined by subtracting the elastic line (generated by integrating in a narrow  $Q$  range around the first Bragg peak), linearly interpolating the data where elastic scattering was dominant (up to 8 meV for low-temperature data and 5 meV for the high-temperature data), and by using the ISDOS10 [28,29] software which utilizes the Fourier-log method to provide the DPS in the incoherent scattering approximation [30,31] after correcting for multiphonon contributions. This procedure iteratively produces a self-consistent solution starting from a best-guess density of phonon states, and does not require prior knowledge of materials parameters such as the atomic displacement parameters. As input, we utilized an average momentum transfer of  $\langle Q \rangle \sim 6.5 \text{ \AA}^{-1}$  corresponding to the instrument geometry and incident energy, which is

equivalent to a recoil energy,  $E_R = \frac{(\hbar Q)^2}{2M} \sim 0.5 \text{ meV}$ , where  $M = 192.2 \text{ amu}$ . The energy range of 0–30 meV was used to calculate the DPS. We also utilized a 60% partial spectral deconvolution by the instrument resolution function. We only use the phonon creation part  $S(E > 0)$  because the instrumental resolution rapidly degrades for  $E < 0$ . Note that the sample does show evidence of texture [see Fig. 5(d) in Appendix]. However, since iridium has a cubic unit cell and because we are sampling a large number of Brillouin zones, the DPS is not significantly affected.

### III. CALCULATION DETAILS

Density functional theory calculations were performed using the software package QUANTUM ESPRESSO [32] with the local-density approximation (LDA) functional of Perdew and Zunger [33] and ultrasoft pseudopotentials [34]. To obtain converged force constants, minimum wave-function and density cutoffs of 40 and 500 Ry, respectively, were used with an electronic cold smearing parameter of 0.02 Ry and a Monkhorst-Pack  $33 \times 33 \times 33$  grid for the first Brillouin-zone sampling. The phonon frequencies were calculated using density functional perturbation theory [35] on a  $12 \times 12 \times 12$  grid in reciprocal space, and the interatomic force constants were subsequently obtained by interpolation. The DPSs were calculated using a  $100 \times 100 \times 100$  uniform grid in reciprocal space and a Lorentzian broadening parameter of 0.3 meV. The phonon properties at finite temperatures were computed using the quasiharmonic approximation, with temperature-

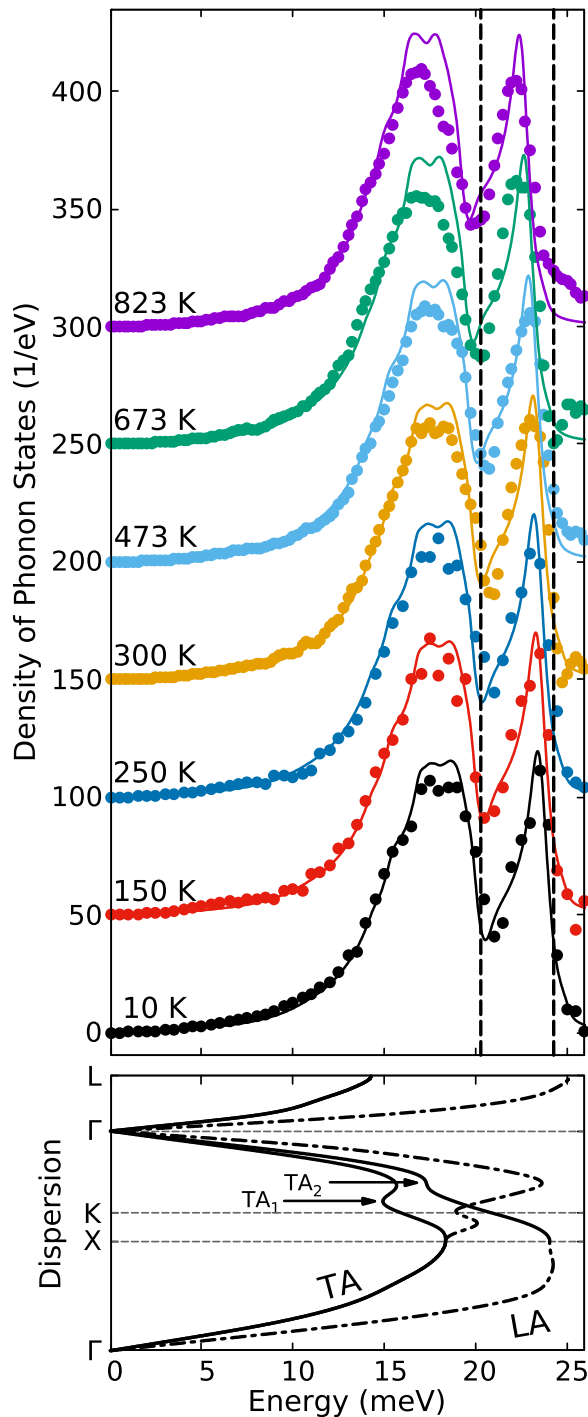


FIG. 2. Top: Density of phonon states (DPS) of iridium for  $10 \text{ K} < T < 823 \text{ K}$ . Solid lines are quasiharmonic DFT calculated DPS (discussed below). Dashed vertical lines correspond to 10-K edges of the experimental TA (lower  $E$ ) and LA (higher  $E$ ) modes. Bottom: Calculated phonon dispersion illustrating both transverse- and longitudinal-acoustic modes across several symmetry points. TA<sub>1</sub> and TA<sub>2</sub> refer to when the two transverse modes are nondegenerate in the  $\Gamma$ -K-X [110] direction. Experimental and calculated DPS are shown separately for clarity in Fig. 8 in Appendix.

dependent lattice constants taken from reported measurements [20]. Including spin-orbit coupling gives a relatively minor

softening of the phonon modes (see Fig. 11 in Appendix). We also explored the effects of functional type and anharmonicity in determining the calculated phonon dispersion and DPS. Using the measured low-temperature and 300-K lattice parameters, the generalized gradient approximation (GGA) gives generally harder phonons ( $\sim 0.3 \text{ THz}$  maximum) compared to LDA and measured values. Calculated anharmonic line shifts were negligible in the temperature range considered. Broadening of the phonon modes from three-phonon anharmonic interactions [36] also had little effect on the overall DPS besides slightly broadening the LA peak with increasing temperature (see Fig. 11).

QUANTUM ESPRESSO input files and harmonic interatomic force constants (IFCs) for the Perdew-Zunger calculation without spin-orbit interactions and relaxed structure are given in the Supplemental Material [37]; other information can be provided upon request.

## IV. RESULTS

### A. Absorption correction

When necessary, but not too large, neutron absorption can be handled automatically by data reduction software. However, since the detector coverage at ARCS extends significantly out of the scattering plane, adequate absorption corrections are not currently implemented. We have attempted to correct the spectra using the “flat plane” absorption correction method implemented in the MSlice (DAVE) program [27], which led to some improvement in the data, but ultimately failed because of the very thin plate geometry of the sample, the lack of integration of beam divergence, and the lack of correction for out-of-plane scattering. As a symptom, the detailed balance of Stokes and anti-Stokes processes was noticeably violated even after absorption correction (see Fig. 7 in Appendix). Instead, we developed and applied another correction technique that relies only on the  $S(E)$  data and not on details of the instrument or sample geometry.

Before absorption correction, the scattering functions  $S(E)$  exhibit unphysical ratios of peak intensity between the Stokes and anti-Stokes processes (positive and negative energy side of the elastic line, where positive corresponds to neutron energy loss); see Fig. 1(c). Ultimately, for *all* temperatures, the positive energy side is expected to exhibit a larger peak intensity than the negative side due to the principle of detailed balance. However, the opposite is noticeably observed at the highest temperatures. Here, we quantify the detailed balance as the scattering function divided by the same function inverted on the energy axis,  $[\frac{S(E>0)}{S(E<0)} \exp(\frac{-E}{k_B T})]$ , which represents the ratio of phonon creation over annihilation. With the  $\exp(\frac{-E}{k_B T})$  temperature correction, the detailed balance should, ideally, graphically fall along a horizontal line of unity value. Instead, the detailed balance of all the INS spectra collected from ARCS is slanted [Fig. 1(a)], indicative of the large neutron absorption of iridium, i.e., the neutrons that have lost energy in a phonon creation process are severely absorbed relative to those that have gained energy in a phonon annihilation process. If not corrected, this results in an imbalance in the overall peak areas in the density of phonon states (see Fig. 6 in Appendix), where the peak heights of the longitudinal

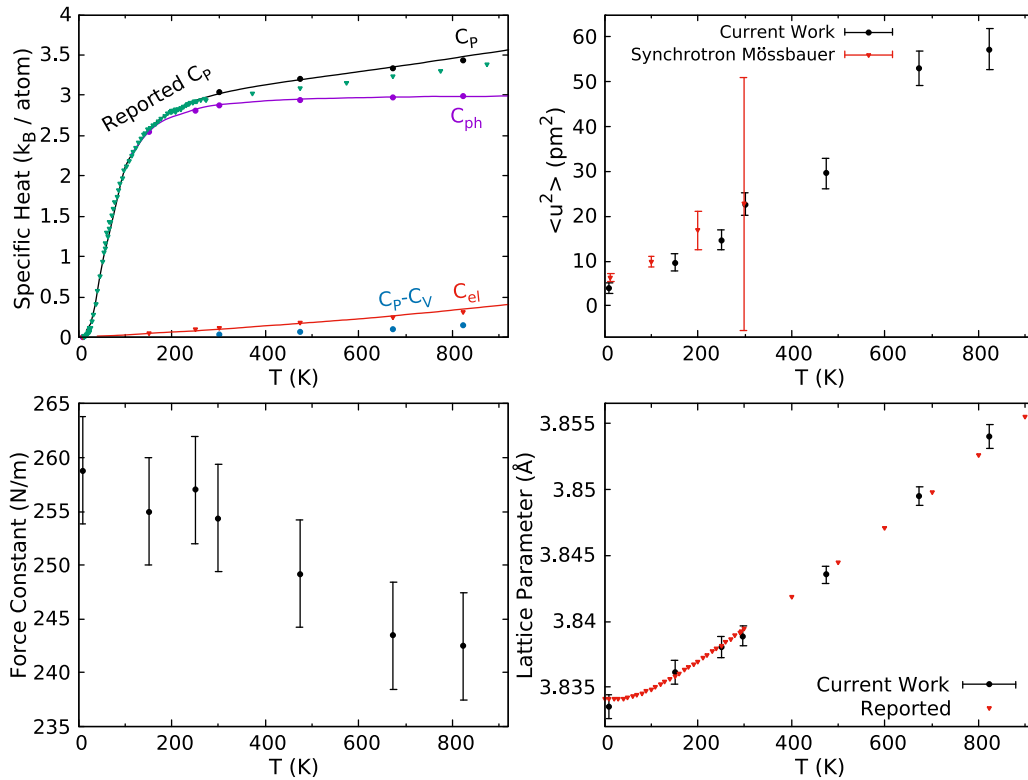


FIG. 3. (a) Heat capacity of iridium. Solid lines are calculated values from Ref. [12]. Green ( $C_p$ ) and red ( $C_{el}$ ) inverted triangles are reported values [24,38] and circles are values from the current work (see Table I). (b) Mean atomic displacement  $\langle u^2 \rangle$  of iridium across multiple temperatures. Black circles are data from the current work and inverted red triangles are from nuclear forward scattering data in Ref. [46]. (c) Force constant values of iridium. (d) Lattice constants of iridium extracted from the current work (black circles) and reported values (inverted red triangles) [20].

acoustic (LA) and transverse acoustic (TA) modes should be roughly equal. The apparent violation of the detailed balance principle provides an opportunity for an effective absorption correction procedure. Because the difference of the creation vs annihilation of phonons is essentially an exponential function of temperature, the TA mode regions [white regions in Fig. 1(a)] of the detailed balance were fit with a simple function  $\exp(-aE)$ , where  $a$  was determined using the 300-K data for which there is no thermometry-related unknown in the temperature. Each scattering function was then corrected by dividing the spectrum by the correction factor  $\exp(-\frac{aE}{2})$  (the factor 2 arises because we correct the scattering function instead of the detailed balance). After correction, the detailed balance was used to verify that the actual temperature of each run was reasonably close to that indicated by thermometry. The result is a flat detailed balance [Fig. 1(b)] and scattering functions with physically correct weighted sides [Fig. 1(d)] for each temperature, effectively correcting the absorption and leading to the correct intensity ratios between the TA and LA phonon peaks when compared to DFT calculations (discussed further below). The resulting temperature-dependent DPS are shown in Fig. 2 and the derived thermodynamic parameters are summarized in Fig. 3 and Table I.

**B. Lattice dynamics from the density of phonon states**

The DPS features two clear peaks corresponding to Van Hove singularities for the TA and LA modes. Note that there

is no clear separation between the singularities generated by the  $TA_1$  and  $TA_2$  modes mostly because these are degenerate along the  $\Gamma-X$  [100] and  $\Gamma-L$  [111] directions. With the absorption correction applied, the area ratio between the peaks is now approximately 2:1, corresponding to the two TA polarizations vs single LA polarization. The vertical dashed lines

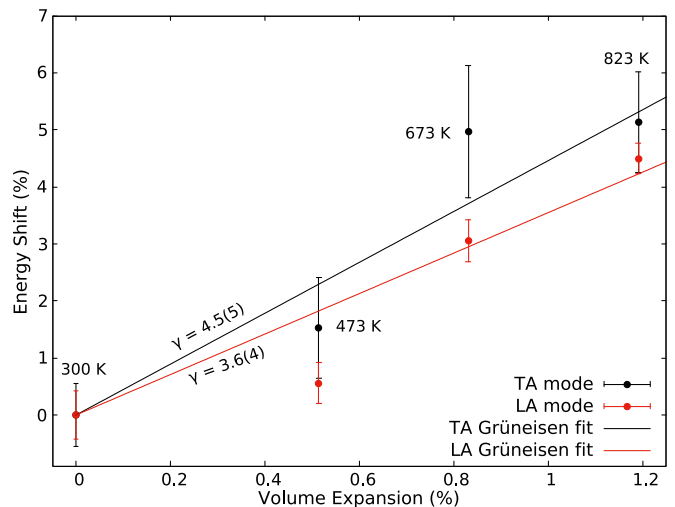


FIG. 4. Relative changes in energy and volume for the TA and LA modes and their linear fits, whose slopes correspond to the microscopic Grüneisen parameters  $\gamma_{TA}$  and  $\gamma_{LA}$ .



TABLE I. Thermodynamic parameters of iridium extracted from DPS.

Temp. (K)	Internal energy (meV)	Force constant (N/m)	Vibrational entropy ( $3k_B$ )	$\langle u^2 \rangle$ ( $\text{pm}^2$ )	Heat cap. ( $C_P$ ) ( $3k_B$ ) <sup>a</sup>	Heat cap. ( $C_{ph}$ ) ( $3k_B$ )	$C_P - C_V$ ( $3k_B$ )	$C_{el}$ ( $3k_B$ ) <sup>b</sup>
10	28.09(3)	259(5)	7.2(3)E-04	3.95(1)		0.002(1)		0.001
150	44.37(4)	255(5)	0.756(1)	9.7(1)		0.848(1)		0.019
250	66.58(4)	257(5)	1.184(1)	15(1)		0.940(1)		0.031
300	79.76(2)	254(5)	1.392(1)	23(1)	1.011	0.959(1)	0.014	0.038
473	117.63(4)	249(5)	1.786(1)	29.6(1.0)	1.065	0.983(1)	0.023	0.060
673	171.69(4)	243(5)	2.197(1)	53.0(1.4)	1.112	0.992(1)	0.035	0.085
823	200.74(4)	242(5)	2.349(1)	57.3(1.4)	1.146	0.994(1)	0.048	0.104

<sup>a</sup>Low-temperature  $C_P$  values are not present due to a lack of low-temperature bulk modulus data.

<sup>b</sup> $C_{el}$  values are calculated from the reported value [38].

in Fig. 2 indicate the peak edges (extremum of the derivative) of both modes at 10 K and reveal how both modes soften with increasing temperature.

From the DPS, we extract thermodynamics quantities, including the phonon specific heat,

$$C_{ph} = 3k_B \int_0^\infty g(E) \frac{(E/k_B T)^2 e^{E/k_B T}}{(e^{E/k_B T} - 1)^2} dE. \quad (1)$$

Here,  $g(E)$  represents the DPS. With this and the reported electronic specific heat values ( $C_{el} = \gamma T$ ;  $\gamma = 0.01634 \text{ J kg}^{-1} \text{ K}^{-2}$ ) determined from  $C_P$  and the Debye temperature  $\theta_D$  [38], we can calculate the heat capacity at constant volume as  $C_V = C_{ph} + C_{el}$ . Further, using the reported density ( $\rho$ ), linear thermal expansion ( $\alpha$ ) [20], and isothermal bulk modulus ( $B_T$ ) values [23] we find  $C_P$  using

$$C_P - C_V = \frac{9B_T \alpha^2 T}{\rho}. \quad (2)$$

These  $C_P$  and  $C_{ph}$  values, along with  $C_{el}$ , are presented in Fig. 3(a) alongside previously reported measured  $C_P$  values and calculated values of  $C_P$ ,  $C_{ph}$ , and  $C_{el}$  [12,24]. While the  $C_{ph}$  data (not including  $C_{el}$ ) line up very well with calculations and reach the expected high-temperature limit of  $\sim 3k_B$ , the  $C_P$  data deviate slightly from the reported values. This is likely due to inconsistent temperature-dependent bulk modulus values, which could lead to an incorrect anharmonic term ( $C_P - C_V$ ).

For 300 K and above,  $B_T$  was obtained from measured values of the shear modulus ( $G$ ), Young's modulus ( $E$ ), and Poisson's ratio ( $\nu$ ), [23] which can be used to calculate  $B_T$  three different ways. This leads to three values: 296, 356, and 371 GPa at 300 K. The 356-GPa value, obtained using  $E$  and  $\nu$ , was chosen since it aligns with the average of all reported room-temperature  $B_T$  values [22,39–45].

A precise determination of the mean atomic displacement ( $\langle u^2 \rangle$ ) is also possible from the DPS at each temperature,

$$\langle u^2 \rangle = \frac{\hbar^2}{2M} \int_0^\infty \frac{g(E)}{E} \coth\left(\frac{E}{2k_B T}\right), \quad (3)$$

where  $M$  is the atomic mass of iridium. The results are displayed in Fig. 3(b) and compare well with those previously

reported by synchrotron Mössbauer spectroscopy [also known as nuclear forward scattering (NFS)] [46,47].

Last, the averaged force constants calculated from the DPS using

$$\langle F \rangle = \frac{M}{\hbar^2} \int_0^\infty g(E) E^2 dE \quad (4)$$

are presented in Fig. 3(c), whereas the vibrational entropy and total internal energy are presented in Fig. 9 in Appendix.

The lattice parameters were determined using a cut along  $S(Q)$  in the  $-2$  to  $2$  meV energy range, from which a polycrystalline diffraction pattern was extracted (see Fig. 10 in Appendix). By fitting the Bragg peak positions in the  $S(Q)$  plot, lattice parameters were extracted at each temperature, which line up reasonably well with reported values from dilatometry [see Fig. 3(d)]. We note however that the uncertainty in the wavelength of the ARCS spectrometer does not allow us to obtain precise lattice constants but allows verification of cross consistency between the lattice constant, detailed balance, and temperature.

From the softening of the LA and TA modes with increasing temperature in Fig. 2 we can quantify anharmonicity. The edge energies of both peaks were extracted from the DPS via the fit shown in Fig. 8 in Appendix. Together, these were used to calculate a microscopic Grüneisen parameter for each mode,

$$\gamma_i = -\frac{V}{E_i} \frac{\partial E_i}{\partial V}, \quad (5)$$

where  $V$  is the cell volume and  $E_i$  is the energy of the specific TA or LA phonon mode. Here, these mode Grüneisen parameters are based on the Van Hove singularities instead of the phonon dispersion and have values of 4.5(5) and 3.6(4) for the TA and LA modes, respectively, fitted to data in the temperature range 300–823 K, as shown in Fig. 4. This is consistent with the force constant data, which display a  $\sim 4\%$  change from 300 to 823 K for a 1% volume change. This agrees qualitatively with previous reports that the TA mode is more sensitive to cell compression than the LA mode [14,48].

In contrast, the macroscopic Grüneisen parameter is evaluated by [49]

$$\gamma = \frac{\alpha B_S}{C_P \rho}, \quad (6)$$

where  $B_S$  is the adiabatic bulk modulus, calculated as

$$B_S = \left( \frac{C_P}{C_V} \right) B_T. \quad (7)$$

$\gamma$  ranges from 2.37 at 300 K to 2.36 at 823 K, which agrees well with published values. Singh reported Grüneisen parameters ranging from 2.35 at 297 K to 2.83 at 1000 K, following a roughly linear trend [21]. Fang *et al.* reported a computed value of 2.54 at 300 K, which drops slightly, but remains relatively constant at elevated temperatures [12]. The Grüneisen parameter quantifies the anharmonicity of the system, as phonon energies are not volume dependent in harmonic systems. Clearly, the macroscopic value is significantly smaller than the individual phononic Grüneisen parameters. This is not unexpected since anharmonic interactions more strongly shift and broaden higher energy phonon modes due to a prevalence of available scattering pathways as determined by conservation of momentum and energy conditions [50].

### C. Quasiharmonic DFT calculations

The quasiharmonic DPS calculations provide a reasonable model of the DPS of iridium at low temperatures, as shown in Fig. 2. Here, the quasiharmonic approximation

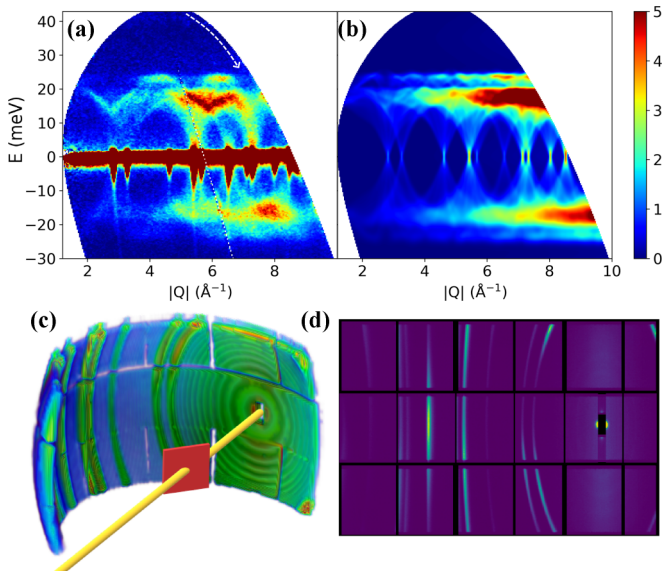


FIG. 5. (a) Measured and (b) calculated  $S(Q, E)$  of iridium at 300 K. Notice the partial disagreement in intensities due to absorption and preferred orientation. The dashed white arrow in (a) highlights the absorption shadow due to the flat plate geometry. (c) Illustration of sample geometry relative to the ARCS detectors, indicating the  $45^\circ$  relative angle of the sample sheet (red) to the incident neutrons (yellow). (d) Detector image of the 300-K data with a linear intensity scale, some preferred orientation is visible, e.g., in the large intensity of the [004] Debye-Scherrer ring (second column, middle detector bank).

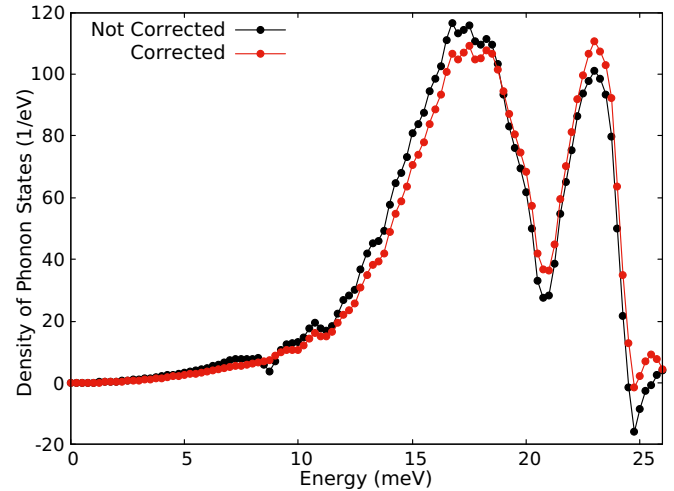


FIG. 6. Comparison of absorption-corrected (red) and non-absorption-corrected (black) iridium DPS at 300 K.

assumes that the phonon dispersion only relies on temperature through the change in volume. However, at higher temperatures, the model begins to deviate from measurements, which soften much more with temperature, especially for the TA modes. This indicates that the temperature dependence of phonon frequencies in iridium cannot be attributed only to variations in the lattice constant. The enhanced softening may be due to other factors such as phonon-phonon or phonon-electron renormalization, or possibly just a frequency-dependent phonon-phonon broadening due to anharmonic scatterings. These possibilities are not explored in the current work as they require single-crystal inelastic scattering data. The calculated DPS without the experimental data using different flavors of LDA, Perdew-Zunger and Perdew-

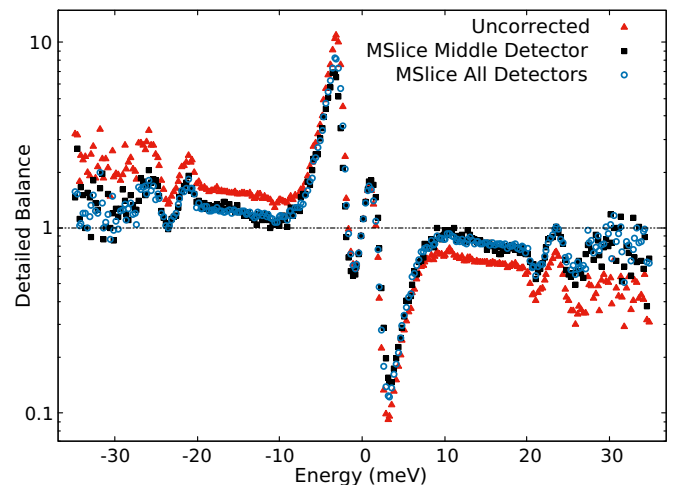


FIG. 7. Detailed balance of 300 K INS data that has been absorption corrected through the MSlice program using a flat plate geometry (parameters: detector angle =  $-39^\circ$ , absorption length = 5.28 mm, thickness = 4 mm). Black squares indicate the data collected from the central bank of detectors, whereas blue circles indicate data collected from the entire range of detectors. The uncorrected data (red triangles) is included for comparison.

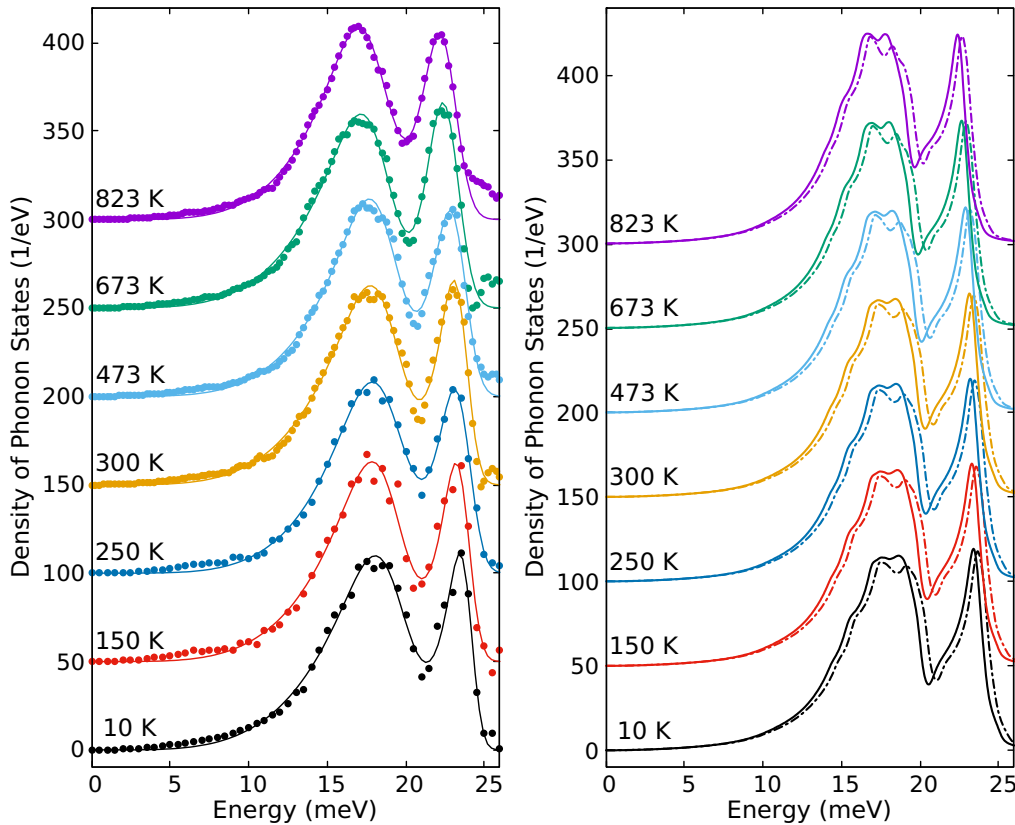


FIG. 8. Left: DPS of iridium at 10–823 K. Solid lines are simple fits using a power function of the energy on the lower energy side weighted by a smooth edge function that cuts off the intensity. This provides a good measure of the cutoff energy for both phonon peaks. Right: Quasiharmonic approximation DPS calculation using the Perdew-Zunger LDA (solid lines) and the Perdew-Wang LDA (dashed lines). Vertical dashed lines correspond to 10-K edges of the Perdew-Zunger TA and LA modes.

Wang, are given in Fig. 8 (right) in Appendix. Including spin-orbit coupling with the 300-K Perdew-Zunger calculation further softens both modes (see Fig. 12 in Appendix). The closest match with experiment at 300 K is obtained using only the Perdew-Zunger LDA with no spin-orbit coupling. The approximate mode Grüneisen parameters obtained from the same procedure as utilized for the experimental data for the calculated modes are 2.72(2) for the TA mode and 2.89(2) for the LA mode (see Fig. 13 in Appendix), which are broadly consistent with the previously calculated Grüneisen parameters.

## V. CONCLUSION

Iridium is notoriously difficult to measure via inelastic neutron scattering due to its large neutron absorption. A data-intrinsic approach to correct the large absorption has been successfully applied to extract vibrational properties of this surprisingly challenging material. We have reported temperature-dependent density of phonon states of iridium from 10 to 823 K and extracted thermodynamic properties from these, including experimental Grüneisen parameters. The extracted heat capacities, atomic displacement values, and lattice parameters are in good agreement with previously reported values. In contrast, the calculated microscopic Grüneisen parameters are much larger than previously

reported, whereas the macroscopic Grüneisen parameters are slightly lower. The current study is a stepping stone to collecting temperature-dependent phonon dispersion relations for the purpose of a momentum resolved study of the strong electron-phonon coupling phenomena in this material.

## ACKNOWLEDGMENTS

Inelastic neutron scattering work by D.H.M., R.P.H., and M.E.M., and DFT calculations by S.T. and L.L. were supported by the U.S. Department of Energy, Office of Science, Office of Basic Energy Sciences, Materials Sciences and Engineering Division. We thank P. Alexeev and I. Sergeev for fruitful discussions. A portion of this research (INS at ARCS) used resources at the Spallation Neutron Source, a DOE Office of Science User Facility operated by Oak Ridge National Laboratory.

## APPENDIX

Additional information pertaining to the details of the method of absorption correction are presented in Figs. 5–7. Fits to the experimental DPS and comparisons of different quasiharmonic DPS calculations are shown in Fig. 8. Plots of the vibrational entropy and internal energy are presented in Fig. 9, whereas the related equations for calculating these values from the DPS are presented as Eqs. (A1) and

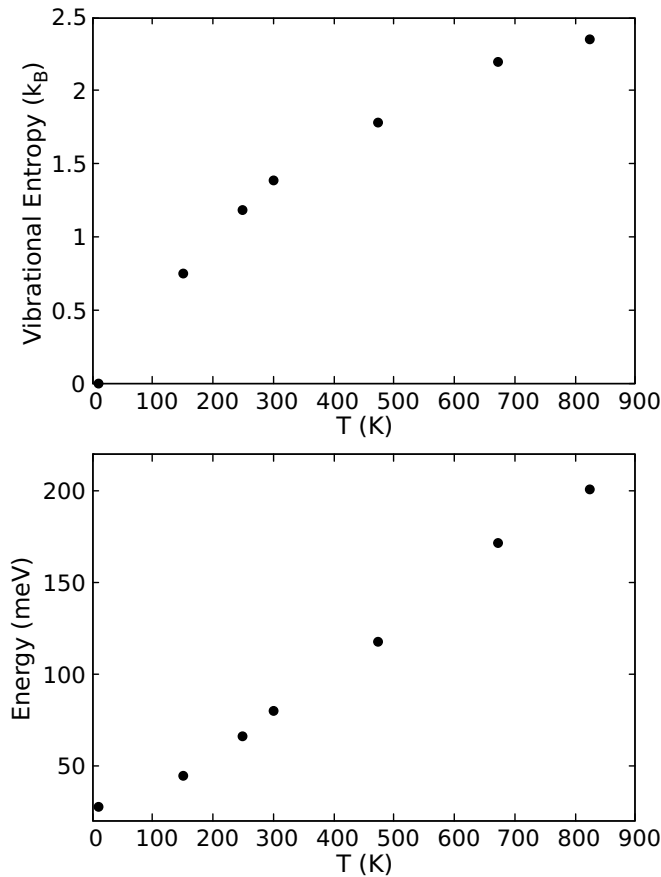


FIG. 9. (Top) Vibrational entropy and (bottom) internal energy of iridium calculated directly from the DPS by Eqs. (A1) and (A2), respectively.

(A2). The diffraction pattern from the ARCS instrument is presented in Fig. 10. Lastly, additional figures concerning

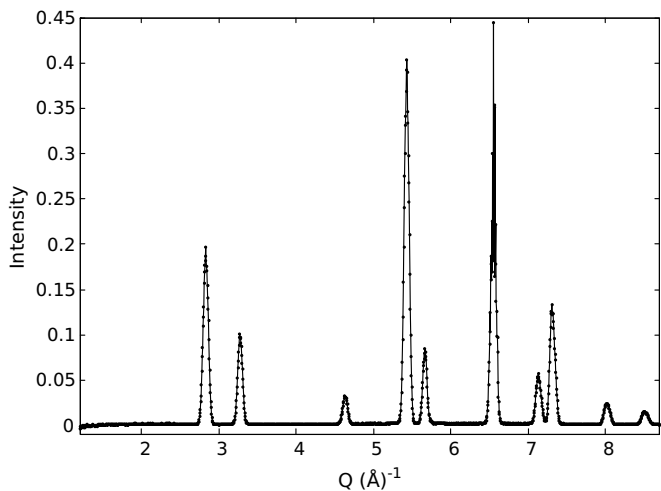


FIG. 10. Diffraction pattern of Ir at 300 K using the ARCS data integrated in an energy range of  $-2$  to  $2$  meV. Some combined preferential orientation leads to deviation relative to the powder average.

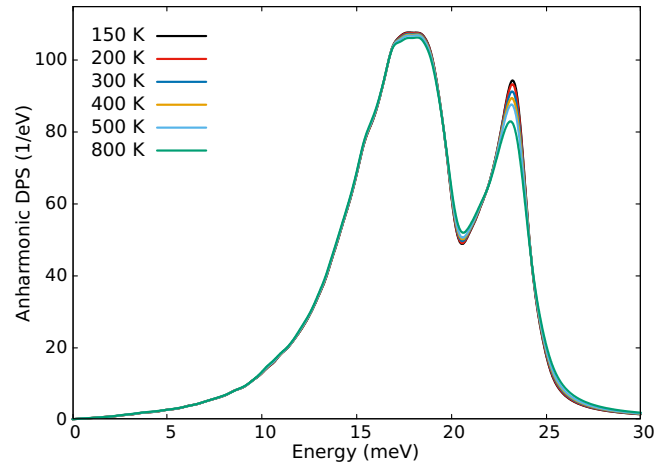


FIG. 11. Calculated anharmonic DPS of iridium.

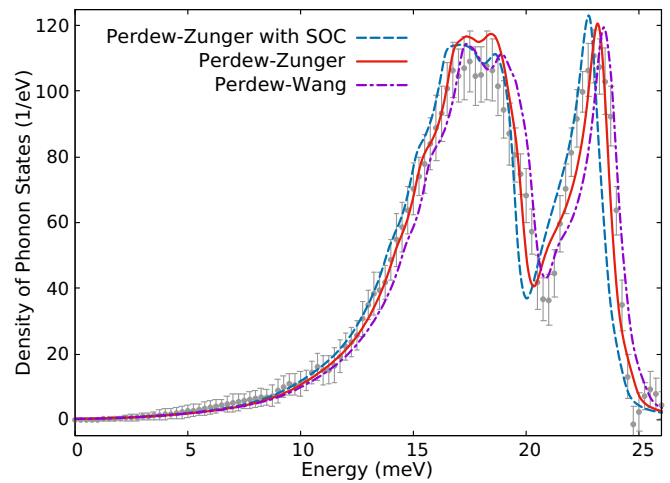


FIG. 12. Comparison of Perdew-Wang (purple dashed line), Perdew-Zunger (red solid line), and Perdew-Zunger with spin-orbit coupling (blue dashed line) calculated iridium DPS at 300 K with experimental data (gray points with error bars).

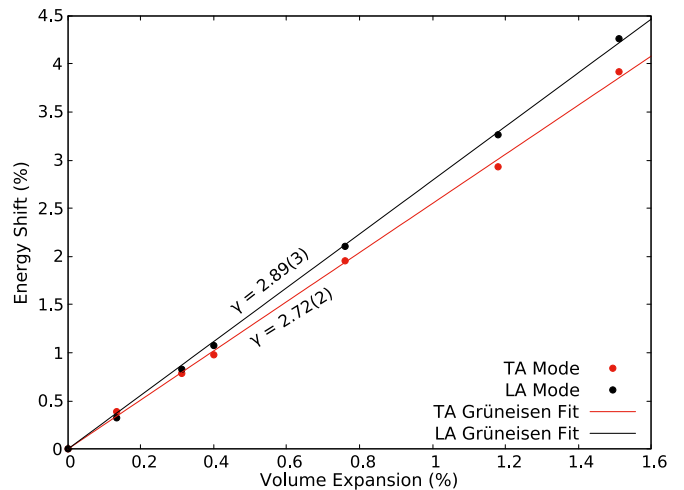


FIG. 13. Mode Grüneisen parameters of the quasiharmonic DFT calculations based on the energy of the edge of each mode. The same fit function as used for the experimental data was used. Percentage changes are based on differences from the 0-K simulation.



anharmonic and quasiharmonic DFT calculations are presented in Figs. 11–13.

$$S_{ph} = 3k_B \int_0^\infty g(E) \left[ \frac{e^{E/k_B T} + 1}{e^{E/k_B T} - 1} \frac{E/k_B T}{2} - \ln(e^{E/k_B T} - e^{-E/k_B T}) \right] dE, \quad (A1)$$

$$U = \frac{3}{2} \int_0^\infty g(E) E \frac{e^{E/k_B T} + 1}{e^{E/k_B T} - 1} dE. \quad (A2)$$

- 
- [1] V. V. Nemoshkalenko, V. Y. Milman, A. V. Zhalko-Titarenko, V. N. Antonov, and Y. L. Shitikov, *JETP Lett.* **47**, 245 (1988).
- [2] A. S. Ivanov, M. I. Katsnelson, A. G. Mikhin, Y. N. Osetskii, A. Y. Romyantsev, A. V. Trefilov, Y. F. Shamaev, and L. I. Yakovenkova, *Philos. Mag.* **B 69**, 1183 (1994).
- [3] R. Heid, K. P. Bohnen, K. Felix, K. M. Ho, and W. Reichardt, *J. Phys.: Condens. Matter* **10**, 7967 (1998).
- [4] R. G. Lange and W. P. Carroll, *Energy Convers. Manag.* **49**, 393 (2008).
- [5] V. F. Sears, E. C. Svensson, and B. M. Powell, *Can. J. Phys.* **73**, 726 (1995).
- [6] J. Trampenau, W. Petry, and C. Herzig, *Phys. Rev. B* **47**, 3132 (1993).
- [7] M. Kresch, M. Lucas, O. Delaire, J. Y. Y. Lin, and B. Fultz, *Phys. Rev. B* **77**, 024301 (2008).
- [8] J. G. Rau, E. K.-H. Lee, and H.-Y. Kee, *Annu. Rev. Condens. Matter Phys.* **7**, 195 (2016).
- [9] E. M. Pärschke, K. Wohlfeld, K. Foyevtsova, and J. van den Brink, *Nat. Commun.* **8**, 686 (2017).
- [10] S. Zhou, K. Jiang, H. Chen, and Z. Wang, *Phys. Rev. X* **7**, 041018 (2017).
- [11] V. N. Antonov, V. Y. Milman, V. V. Nemoshkalenko, and A. V. Zhalko-Titarenko, *Z. Phys. B: Condens. Matter* **79**, 223 (1990).
- [12] H. Fang, B. Liu, M. Gu, X. Liu, S. Huang, C. Ni, Z. Li, and R. Wang, *Phys. B (Amsterdam, Neth.)* **405**, 732 (2010).
- [13] J. K. Baria, *Acta. Phys. Slovaca* **53**, 177 (2003).
- [14] J. K. Baria, *Czech. J. Phys.* **52**, 969 (2002).
- [15] X. Ren, S. Chen, M. Xie, S. Wang, J. Hu, S. Wang, M. Li, and J. Chen, *Int. J. Mod. Phys. B* **29**, 1550220 (2015).
- [16] M. Z. S. Ahmed, M. Shakil, and M. A. Choudhary, *Condens. Matter Phys.* **18**, 23601 (2015).
- [17] A. Dal Corso, *J. Phys.: Condens. Matter* **25**, 145401 (2013).
- [18] M. J. Cawkwell, D. Nguyen-Manh, D. G. Pettifor, and V. Vitek, *Phys. Rev. B* **73**, 064104 (2006).
- [19] N. Singh, *Pramana* **52**, 511 (1999).
- [20] J. W. Arblaster, *Platinum Met. Rev.* **54**, 93 (2010).
- [21] H. P. Singh, *Acta. Cryst.* **A24**, 469 (1968).
- [22] Y. Cerenius and L. Dubrovinsky, *J. Alloys Compd.* **306**, 26 (2000).
- [23] J. Merker, D. Lupton, M. Töpfer, and H. Knake, *Platinum Met. Rev.* **45**, 74 (2001).
- [24] Y. S. Touloukian and E. H. Buyco, *Thermophysical Properties of Matter* (IFI/Plenum, New York, 1970), Vol. 4.
- [25] D. L. Abernathy, M. B. Stone, M. J. Loguillo, M. S. Lucas, O. Delaire, X. Tang, J. Y. Y. Lin, and B. Fultz, *Rev. Sci. Instrum.* **83**, 015114 (2012).
- [26] J. L. Niedziela, R. Mills, M. J. Loguillo, H. D. Skorpenske, D. Armitage, H. L. Smith, J. Y. Y. Lin, M. S. Lucas, M. B. Stone, and D. L. Abernathy, *Rev. Sci. Instrum.* **88**, 105116 (2017).
- [27] R. T. Azaiah, L. R. Kneller, Y. Qiu, P. L. W. Tregenna-Piggott, C. M. Brown, J. R. D. Copley, and R. M. Dimeo, *J. Res. Natl. Inst. Stand. Technol.* **114**, 341 (2009).
- [28] I. Sergeev, 2001 (private communication).
- [29] V. G. Kohn and A. I. Chumakov, *Hyperfine Interact.* **125**, 205 (2000).
- [30] J. Dawidowski, F. J. Bermejo, and J. R. Granada, *Phys. Rev. B* **58**, 706 (1998).
- [31] M. E. Manley, R. J. McQueeney, B. Fultz, R. Osborn, G. H. Kwei, and P. D. Bogdanoff, *Phys. Rev. B* **65**, 144111 (2002).
- [32] P. Giannozzi, S. Baroni, N. Bonini, M. Calandra, R. Car, C. Cavazzoni, D. Ceresoli, G. L. Chiarotti, M. Cococcioni, I. Dabo, A. Dal Corso, S. de Gironcoli, S. Fabris, G. Fratesi, R. Gebauer, U. Gerstmann, C. Gougousis, A. Kokalj, M. Lazzeri, L. Martin-Samos *et al.*, *J. Phys.: Condens. Matter* **21**, 395502 (2009).
- [33] J. P. Perdew and A. Zunger, *Phys. Rev. B* **23**, 5048 (1981).
- [34] A. M. Rappe, K. M. Rabe, E. Kaxiras, and J. D. Joannopoulos, *Phys. Rev. B* **41**, 1227 (1990).
- [35] S. Baroni, S. de Gironcoli, A. Dal Corso, and P. Giannozzi, *Rev. Mod. Phys.* **73**, 515 (2001).
- [36] A. A. Maradudin and A. E. Fein, *Phys. Rev.* **128**, 2589 (1962).
- [37] See Supplemental Material at <http://link.aps.org/supplemental/10.1103/PhysRevMaterials.4.113608> for QE input files and harmonic IFCs for relaxed structure using an LDA Perdew-Zunger pseudopotential without spin-orbit coupling.
- [38] E. S. R. Gopal, *Specific Heats at Low Temperatures* (Plenum, New York, 1966), pp. 61–63.
- [39] R. E. MacFarlane, J. A. Rayne, and C. K. Jones, *Phys. Lett.* **20**, 234 (1966).
- [40] R. N. Singh and I. Ali, *Int. J. Appl. Phys. Math.* **3**, 275 (2013).
- [41] H.-G. Purwins, H. Hieber, and E. Labusch, *Phys. Status Solidi* **11**, K63 (1965).
- [42] V. Monteseguro, J. A. Sans, V. Cuartero, F. Cova, I. A. Abrikosov, W. Olovsson, C. Popescu, S. Pascarelli, G. Garbarino, H. J. M. Jönsson, T. Irifune, and D. Errandonea, *Sci. Rep.* **9**, 8940 (2019).
- [43] S. S. Hecker, D. L. Rohr, and D. F. Stein, *Metall. Trans. A* **9**, 481 (1978).
- [44] K. V. Yusenko, S. Khandarkhaeva, T. Fedotenko, A. Pakhomova, S. A. Gromilov, L. Dubrovinsky, and N. Dubrovinskaia, *J. Alloys Compd.* **788**, 212 (2019).
- [45] L. Burakovsky, N. Burakovsky, M. J. Cawkwell, D. L. Preston, D. Errandonea, and S. I. Simak, *Phys. Rev. B* **94**, 094112 (2016).
- [46] P. Alexeev, Ph.D. thesis, University of Hamburg, 2017.

- [47] P. Alexeev, O. Leupold, I. Sergueev, M. Herlitschke, D. F. McMorrow, R. S. Perry, E. C. Hunter, R. Röhlberger, and H.-C. Wille, *Sci. Rep.* **9**, 5097 (2019).
- [48] V. N. Antonov, V. Y. Milman, V. V. Nemoshkalenko, and A. V. Zhalko-Titarenko, *Z. Phys. B: Condens. Matter* **79**, 233 (1990).
- [49] G. Grimvall, *Thermophysical Properties of Materials* (North-Holland, Amsterdam, 1999).
- [50] J. M. Ziman, *Electrons and Phonons: The Theory of Transport Phenomena in Solids*, Oxford Classic Texts in the Physical Sciences (Oxford University Press, Oxford, London, 1960).